An efficient ERR-Cohesive method for the modelling of delamination propagation with large elements

(article starts on next page)

An efficient ERR-Cohesive method for the modelling of delamination propagation with large elements

Pierre M. Daniel [a,b,*], Johannes Främby [c], Martin Fagerström [d], Pere Maimí [b]

[a] Btech[c] - Barcelona Technical Center S.L., Calle Juan de la Cierva N° 2, 08760 Martorell, Spain
[b] AMADE, Mechanical Engineering and Industrial Construction Department, University of Girona, Carrer Universitat de Girona 4, E-17003 Girona, Spain
[c] DYNAmore Nordic AB, Gothenburg, Sweden
[d] Department of Industrial and Materials Science, Division on Material and Computational Mechanics, Chalmers University of Technology, Gothenburg, Sweden

ARTICLE INFO

ABSTRACT

The accurate modelling of delamination propagation is necessary to numerically assess the behaviour of layered materials during failure. Many available methods present computational limitations for large structures. Conventional cohesive zone modelling implies using a fine mesh, typically smaller than 1.0 mm, since several elements are needed inside the fracture process zone. This article presents an ERR-Cohesive method to model delamination in elements larger than the fracture process zone. The crack propagation is determined with an estimation of the energy release rate by means of the virtual crack closure technique. To progressively open the crack along the element length, a nodal cohesive law is introduced. The novel cohesive formulation allows to smoothly release the interface while dissipating the appropriate amount of energy. Accurate results have been obtained in double cantilever beam, end-notched flexure and mixed-mode bending tests with regular and irregular meshes for element lengths from 2 mm to 8 mm.

1. Introduction

The introduction of composite materials into the transportation industries has created a need for the accurate modelling of the damaging process of Fibre-Reinforced Polymers (FRPs). Accurately capturing delamination is essential as it is one of the main phenomena occurring during the failure of such materials. Using a computationally efficient modelling method is critical to fulfil the industry standards of large structures designed in relatively short development cycles.

The use of Cohesive Zone Modelling (CZM) is currently the most popular method to capture delamination growth accurately. In such modelling, the material degradation in the Fracture Process Zone (FPZ) is described by traction–separation interface laws [1,2], which requires a well refined FPZ; a minimum of 3 elements in the FPZ can be found as recommendation in the literature [3]. Unfortunately, when it comes to brittle interfaces, such as between composite laminae, the FPZ is typically smaller than 1 mm. Consequently, this leads to the necessity of using a fine discretisation to model delamination. In order to alleviate this higher computational cost, Turon et al. [3] have proposed to artificially increase the size of the FPZ by reducing the interface strength. This is effective to some extent, but the accuracy rapidly decreases with larger element lengths. Acceptable results can be

obtained with a mesh size of about 1 mm [4]. Nonetheless, this level of refinement is still computationally prohibitive for large models in the industry.

Another limitation of the CZM comes from the artificial stiffness introduced in order to capture the damage initiation by means of a stress-based criterion. On the one hand, this artificial stiffness needs to be high enough to avoid adding unrealistic compliance to the model [3]. On the other hand, this high stiffness can lead to a small stable time step, which further increases the computational cost of CZM. For these reasons, CZM is usually discarded in the industry when it comes to large structures, especially under dynamic loads.

Previous to the introduction of CZM, many authors had been relying on the estimation of the Energy Release Rate (ERR) in order to assess crack propagation of brittle interfaces. Several methods can be found, either expressing directly the ERR as a function of the applied loads [5] or using the stress intensity factor [6,7]. The J-integral method initially proposed by Rice [8] is also commonly used to evaluate the ERR [9,10]. Finally, the crack closure integral introduced by Irwin [11] has led to the Virtual Crack Closure Technique (VCCT) developed by Rybicki et al. [12], which has been used extensively, see [13]. Compared to

Nomenclature

A	Area to open when propagating the crack
A_e	Element area at the crack interface
a	Crack length
a_0	Initial crack length for DCB, ENF and MMB specimens
B	Mixed-mode ratio
b	Coefficient in the expression of the stable time step
C	Linear shape correction factor
c	Lever length for the MMB tests
c_I, c_{II}	Shape correction factors in mode I (normal opening) and mode II (shear opening)
D	Damage variable of the cohesive law
d	Damage function of the cohesive law
E	Young's modulus
F	Interfacial force at the crack tip
F^-, F^+	Allocated internal forces at the lower and upper nodes of a tied node pair
F_I, F_{II}	Interfacial forces in mode I and mode II
F_I^0, F_{II}^0	Interfacial forces at which the critical ERR has been met
f^-, f^+	Internal elemental forces of the lower and upper sub-laminates
$\mathcal{G}$	Energy dissipated by the cohesive law
G	Shear modulus
G_c	Critical fracture toughness
G_T	Total energy release rate
G_I, G_{II}	Energy release rates in mode I and mode II
G_{Ic}, G_{IIc}	Critical fracture toughnesses
h	Substrate thickness for DCB, ENF and MMB specimens
k_p	Penalty stiffness
k_I, k_{II}	Stiffnesses of the cohesive law in mode I and mode II
k_I^0, k_{II}^0	Initial stiffnesses of the cohesive law
L	Sample half-span length for DCB, ENF and MMB specimens
l	Element length
m	Effective mass
m^-, m^+	Nodal masses associated with the lower and upper nodes of a tied node pair
P	Loading force
t	Current time
u^-, u^+	Displacements of the lower and upper nodes of a tied node pair
X_I, X_{II}	Interface strengths of the cohesive law in mode I and mode II
Δ	Interfacial opening
Δ_I, Δ_{II}	Openings in mode I and mode II
$\Delta_I^*, \Delta_{II}^*$	Openings adapted to account for the offset
$\Delta_I^f, \Delta_{II}^f$	Failure openings when assuming linear softening
$\Delta_I^{max}, \Delta_{II}^{max}$	Maximum openings
$\Delta_I^{offset}, \Delta_{II}^{offset}$	Offset openings
δ	Loading displacement
$\delta t_I, \delta t_{II}$	Cohesive stable time steps in mode I and mode II
η	Exponent for the Benzeggagh–Kenane equation
θ^0	Crack tip opening angle
κ^-, κ^+	Mass ratios of the lower and upper nodes of a tied node pair
ν	Poisson's ratio
ρ	Density

CZM, these ERR-based methods do not aim to reproduce the phenomenon occurring in the FPZ. They usually assume that the interface is brittle leading to a negligible FPZ size where the assumption of Linear Elastic Fracture Mechanics (LEFM) can be applied. Since they depend on the ERR instead of the interface elemental stresses, these methods are suitable for larger elements.

However, these ERR-based methods lack two advantages that CZM has. Firstly, they cannot usually predict crack initiation as they rely on an initial crack to be present in order to estimate if it will propagate further. Secondly, they lack a damage evolution model able to absorb the energy resulting from the progressive propagation of the crack along the element length. In other words, when the ERR predicts crack growth, the crack progresses instantaneously of a distance corresponding to the length of one element. As such, the ERR-based methods do not account for the proper conversion of the stored elastic energy into fracture energy associated with the extension of the crack. This sudden change in the equilibrium leads to either convergence issues associated to high discontinuities under static loads [14–16], or uncontrollable (and unphysical) vibrations under dynamic loads. As a consequence, for ERR-based methods, a model describing the actual fracture process has to be added in order for the crack to open in a controlled and accurate way.

The present article focusses on the efficient modelling of the delamination propagation once a crack has been initiated. Inspired by the work from Mabson et al. [16,17], the proposed ERR-Cohesive (ERRC) method uses an ERR estimation as crack propagation criterion and a cohesive damage formulation to model the progressive growth of the crack along the element length. Among the different ERR estimation methods, the VCCT has been chosen for its straightforward application in Finite Element Analysis (FEA). It has proven to provide reliable ERR estimation for the propagation of delamination with large elements [14, 18,19]. When the predicted ERR exceeds the fracture toughness, a cohesive law is introduced at the crack tip nodes to release the interface smoothly. In the present work, a novel damage formulation is used that allows the appropriate amount of energy to be absorbed with elements much larger than the size of the FPZ. The amount of energy to dissipate is determined by the mixed-mode ratio and the area to be opened. Additionally, the formulation does not add initial artificial compliance to the model. Finally, to account for different element lengths ahead and behind the crack front, a novel mode I correction factor for large elements is proposed for the VCCT.

The model has been implemented as a user subroutine in the commercial solver LS-DYNA [20] in the frame of an adaptive modelling strategy previously published [21,22]. The numerical validation has been carried out with standard delamination propagation tests: Double Cantilever Beam (DCB), End-Notched Flexure (ENF) and Mixed-Mode Bending (MMB). The results of the present method are compared to analytical solutions based on LEFM. In the case of the DCB, a comparison with conventional cohesive elements illustrates the modelling limitation of the latter with respect to the present method. The results show the ability of the ERR-Cohesive method to model delamination growth in regular and irregular meshes with element lengths from 2 mm to 8 mm.

2. Model description

In this section, the ERR-Cohesive method is detailed. In the first place, the VCCT serving as a crack propagation criterion is explained. When the ERR reaches the fracture toughness G_c, a cohesive law is introduced at the crack front to model the progressive damage evolution. After presenting the cohesive law, the energy dissipated by this law is derived to motivate the novel damage formulation used. Finally, the considerations needed for the physical model to be implemented numerically are discussed.

2.1. Crack propagation criterion

The aim of the present method is to efficiently model delamination propagation in large models. Although the nucleation of cracks is out of the scope of this article, it is worth noting that a previous work by the authors aimed to develop a method able to detect possible delamination initiation in large models [23]. In the following, it is assumed that a crack has already been opened with the objective to model its growth accurately and efficiently. A three-dimensional configuration is considered; however, the crack is expected to grow in a known direction.

Since the FPZ is expected to be much smaller than the element length, a crack propagation criterion based on interface element stresses would not be accurate. However, due to their brittle nature, the assumption of LEFM can be applied to FRPs layer interfaces. In such cases, the estimation of the ERR presents a reliable crack propagation criterion. The crack grows when the ERR is higher than the fracture toughness G_c.
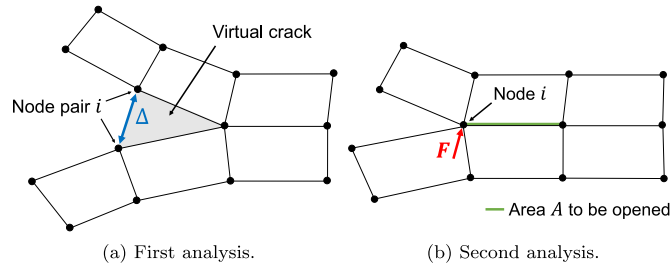

Fig. 1. 2-step crack closure technique. The virtual opening and the interface force are measured in separate analyses.

In the original crack closure method presented by Irwin [11] two analyses were needed. The first one considering the crack opened as in Fig. 1(a), which allows to evaluate the virtual openings $\boldsymbol{\Delta}$. The second one considering the crack closed as in Fig. 1(b), which allows to evaluate the final force $\boldsymbol{F}$ necessary to close the virtual crack. The force $\boldsymbol{F}$ can be computed by making the sum of all the contributions from the elements under the interface at the node i [13]. Note that, due to equilibrium it would be equal to the opposite of the contributions from the elements above the interface. Irwin states that the energy needed to close this virtual crack is equal to the ERR times the area to open, A. It can also be interpreted as a variation of elastic energy per unit area. It leads to the ERR expressed as

$$G_T = \frac{1}{2A} \boldsymbol{F}^\mathrm{T} \boldsymbol{\Delta}. \tag{1}$$

Applying this method to FEA is cumbersome due to the necessity of running each increment twice. To solve this issue, Rybicki [12] proposed to assume self-similar crack propagation in order to evaluate the ERR in a single increment. While the force $\boldsymbol{F}^i$ is still evaluated at the crack tip node i, the opening $\boldsymbol{\Delta}^{i-1}$ is evaluated at a node pair $i-1$ behind the crack tip, see Fig. 2. This method is known as the VCCT.

The ERR mode partitioning is done the following way:

$$G_I = \frac{1}{2A^i} F_I^i \left\langle \Delta_I^{i-1} \right\rangle c_I^i, \tag{2a}$$

$$G_{II} = \frac{1}{2A^i} F_{II}^i \Delta_{II}^{i-1} c_{II}^i, \tag{2b}$$

where G_α is the ERR corresponding to the mode α ($\alpha = I, II$), F_α^i and Δ_α^i are, respectively, the force and the opening in mode α at the node pair i, A^i is the area which will be opened from node pair i to $i+1$ and $\langle \rangle$ are the Macaulay brackets defined as $\langle x \rangle = \frac{1}{2}(x + |x|)$. Finally, c_I^i and c_{II}^i are correction factors, discussed below, which account for the difference between the element length behind l^{i-1} and ahead l^i of the crack tip.
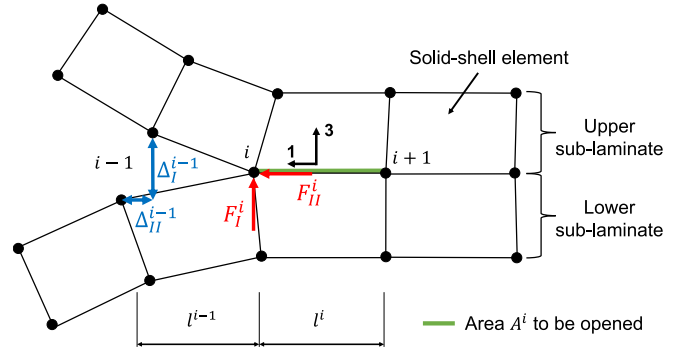

Fig. 2. Single-step VCCT configuration used in the present method. The openings and the interface forces are measured in a single analysis by assuming self-similar crack growth.

In the VCCT, the opening Δ^{i-1} is used as an approximation of the opening Δ^i in the situation where a hypothetical crack would have grown. In the case of a dissimilar element length, the measured opening Δ^{i-1} should be corrected to be representative of the opening at a different length l^i from the crack tip. This shape correction factor is needed to be coherent with the self-similar growth assumption. In the literature, a linear factor

$$C = \frac{l^i}{l^{i-1}} \tag{3}$$

is generally used, as proposed by Krueger [13]. This correction assumes that the openings in mode I and II are linear with respect to the distance from the crack tip. This assumption is reasonable close to the crack-tip, where the crack tip angle dominates the response.

However, it is well-known that the mode I opening is not linearly proportional to the distance from the crack tip beyond a reasonable distance. For the present method to be used with large elements, a better mode I correction factor is therefore needed. With this purpose, a novel correction factor is proposed. Its derivation, based on the Timoshenko beam theory, is presented in Appendix. As a result, a higher order expression for mode I is found, which also includes the crack tip opening angle θ^0. Thus, the shape correction factors are

$$c_I^i = \frac{l^i}{\Delta_I^{i-1}} \theta^0 (1 - C) + C^2, \tag{4a}$$

$$c_{II}^i = C. \tag{4b}$$

Now that the modal ERRs have been defined, the total ERR G_T can be calculated as the sum of the two,

$$G_T = G_I + G_{II}, \tag{5}$$

and the critical fracture toughness G_c can be defined using the Benzeggagh–Kenane equation [24],

$$G_c = G_{Ic} + \left[G_{IIc} - G_{Ic} \right] B^\eta, \tag{6}$$

where G_{Ic} and G_{IIc} are the pure-mode fracture toughnesses, B is the mixed-mode ratio defined as

$$B = \frac{G_{II}}{G_T}, \tag{7}$$

and the exponent η is a parameter to be determined experimentally.

Based on the LEFM assumptions, the crack propagates when the ERR G_T reaches the critical fracture toughness G_c. At this moment, the constraint condition maintaining the node pair i coincident is released.

In the absence of an energy dissipation mechanism the crack propagates suddenly from node pair i to node pair $i + 1$, creating uncontrollable vibrations in dynamic analysis. These artificial vibrations often make the crack to propagate further in a short time, up to the end of the sample. An example of such behaviour is presented in Fig. 3.
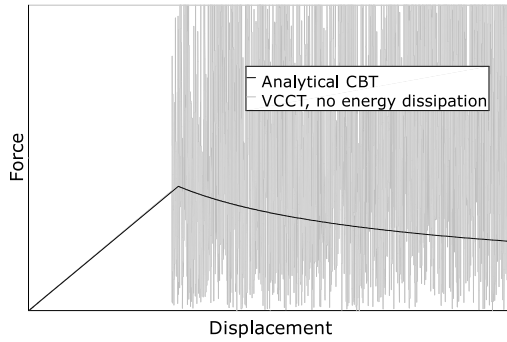

Fig. 3. Example of uncontrollable crack propagation, in dynamic analysis, when the VCCT is used without energy dissipation mechanism. The dimensions of the DCB test and the material used are presented later on in Section 4.1.

In the present method, when the critical ERR is reached, a cohesive law is introduced at node pair i to control the progressive opening of the crack along the entire element length, up to node pair $i + 1$.

2.2. Energy dissipation mechanism

The cohesive law starts in a closed configuration with the node pair maintained coincident by the interface forces F_α^i. Since the following is derived for any given node pair, the superscript i is dropped in the notation. The modal force F_α^i at which the critical ERR has been met becomes F_α^0.

The progressive opening is modelled by degrading the interface forces by means of a damage variable D. This damage formulation must ensure that the dissipated energy corresponds to the opened area through $\mathcal{G} = AG_c$.

The cohesive law is expressed as follows:

$$F_I = \begin{cases} \dfrac{\left| F_I^0 \right|}{\Delta_I^{max}} (1 - D) \langle \Delta_I \rangle & \text{for } \Delta_I > 0 \\ F_I \in \left] -\infty, \left| F_I^0 \right| \right] & \text{for } \Delta_I = 0 \end{cases}, \tag{8a}$$

$$F_{II} = \dfrac{\left| F_{II}^0 \right|}{\Delta_{II}^{max}} (1 - D) \Delta_{II} \quad \text{for } \Delta_{II} \neq 0, \tag{8b}$$

where $\Delta_I^{max} = \max_{\tau \in [0,t]} \langle \Delta_I(\tau) \rangle$ and $\Delta_{II}^{max} = \max_{\tau \in [0,t]} \left| \Delta_{II}(\tau) \right|$ with t being the current time. Furthermore, D is the total damage defined by the function

$$d = (1 - B) \dfrac{\langle \Delta_I \rangle}{\left| \Delta_I^f \right|} + B \left| \dfrac{\Delta_{II}}{\Delta_{II}^f} \right|, \tag{9}$$

which is ensured to be included in the $[0, 1]$ interval by setting

$$D = \max_{\tau \in [0,t]} \left[\min\{1, d(\tau)\} \right]. \tag{10}$$

The mixed-mode ratio B has previously been determined in the ERR estimation and is considered to be constant throughout the energy dissipation. Finally, Δ_α^f is the opening at which the energy AG_α would be consumed by linear softening in mode α:

$$\Delta_\alpha^f = \dfrac{2AG_\alpha}{F_\alpha^0} \tag{11}$$

It is worth noting, by comparing Eqs. (2) and (11), that the value of Δ_α^f is equal to the corrected opening $\Delta_\alpha^{i-1} c_\alpha^i$ at which the VCCT has been triggered. Therefore, if Δ_I and Δ_{II} reach Δ_I^f and Δ_{II}^f, respectively, D

is equal to 1, thus respecting the self-similar growth assumption of the VCCT.

The current stiffness in mode α can be expressed as

$$k_\alpha = \dfrac{\left| F_\alpha^0 \right|}{\Delta_\alpha^{max}} (1 - D), \tag{12}$$

where one can see that the initial stiffness is theoretically infinite due to Δ_α^{max} being null when the cohesive law is introduced. This initial infinite stiffness can be explained physically by the thickness of the modelled interface being null. In order to enable the implementation of this physical model in a FEA software, a formulation presenting a finite initial stiffness is presented in Section 2.5.

A representation of the resulting cohesive law is presented in Fig. 4. Taking the example of a simple pure mode I loading, such as a DCB test, $B = 0$ leads to d being entirely defined by the mode I opening: $d = \frac{\langle \Delta_I \rangle}{\left| \Delta_I^f \right|}$. In this particular case, the softening is linear with respect to the opening Δ_I and will follow the straight line from $(0, F_I^0)$ to $(\Delta_I^f, 0)$ in Fig. 4(a). However, it is important to note that linear softening is not true in general because the damage D is function of both mode I and mode II openings.

More generally, the softening defined by Eqs. (8) and (9) states that both modes are equally degraded and that each mode contributes proportionally to its importance in the ERR into the total damage D. Since the single damage variable D depends on both Δ_I and Δ_{II}, the softening of F_α^0 is not necessarily linear with respect to its associated opening Δ_α. For example, a possible non-linear softening, corresponding to a transition toward higher mixed-mode ratio, is represented by the blue line in Fig. 4. However, also in such non-linear softening, the dissipated amount of energy is AG_c as demonstrated in Section 2.4.

2.3. Mixed-mode behaviour

Conventional cohesive zone modelling, such as that developed by Turon et al. [2,3], reproduces the local phenomenon occurring in the fracture process zone with an evolving mixed-mode ratio B. Although the global mixed-mode ratio may be constant (e.g. 50% in a case of mixed-mode bending), it will not be kept constant locally in the fracture process zone [25]. Referring to Fig. 5, it is clear that its inner part (closest to the intact interface) starts damaging in pure mode II, while the outer part (to the right in the figure) finishes damaging mostly in mode I [25]. Throughout its softening, in order to respect the proper energy dissipation, the cohesive element must endure an average mixed-mode ratio equal to the global mixed mode ratio applied. For the FPZ to be reproduced accurately, sufficiently high refinement has to be employed, typically more than 3 elements inside the cohesive zone are recommended [3].

In the present modelling, where the FPZ is much smaller than the element length, only the outer node pair is carrying the cohesive law. At the same time, the damage law presented here does not model the FPZ, thus it should represent a crack growing along the entire element length, see Fig. 6. Therefore, it would not be relevant to use a conventional cohesive formulation, where the mode mixity is defined by the current opening at the node pair i. For this reason, the mixed-mode B is evaluated by means of the ERR and kept constant throughout the energy dissipation. The important parameter is the amount of energy AG_c to be dissipated for this mixed-mode ratio.

Additionally, in mixed-mode cases, one would observe that the crack tends to open first in pure mode II (similarly to conventional CZM). This motivates for a coupled damage variable where the initial mode II opening allows for mode I softening, thus avoiding locking of the opening Δ_I.

When the damage D reaches significant values (e.g. instant t_b in Fig. 6), one could make the physical interpretation that the crack has grown along part of the element length. However, it should be
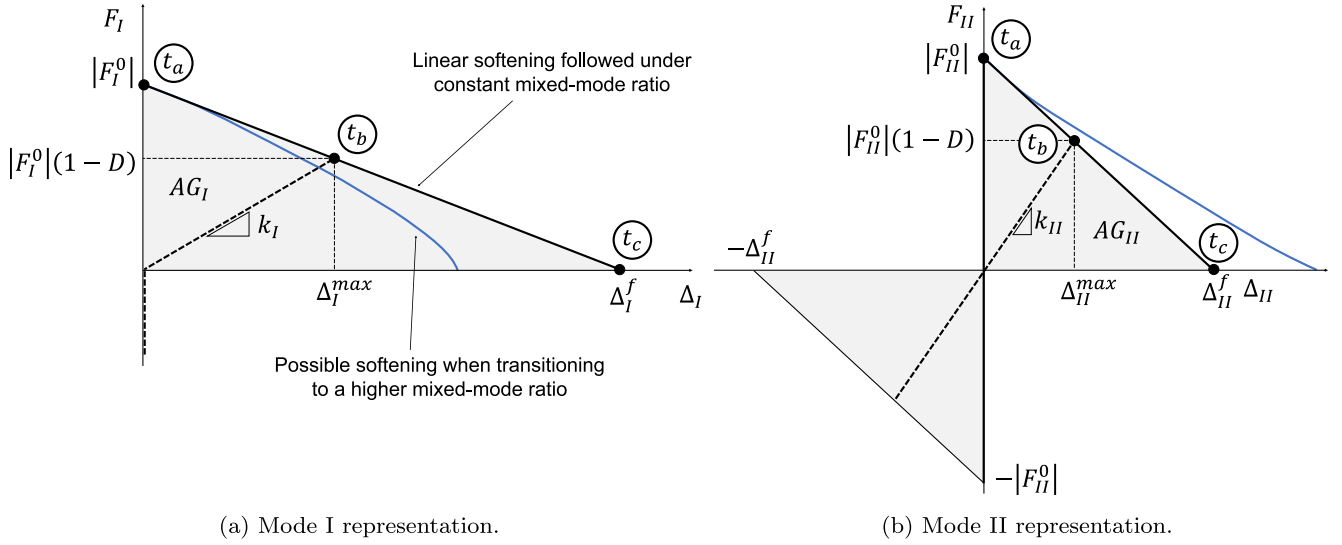
(a) Mode I representation.

(b) Mode II representation.

Fig. 4. Force-opening representation of the cohesive law. The cohesive law is initiated with the forces F_I^0 and F_{II}^0 for which ERR $= G_c$. Under constant mode mixity, the cohesive law follows the straight lines from $(0, F_a^0)$ to $(\Delta_a^f, 0)$. Under variable mode mixity, the path is not linear. It is ensured that the total energy absorbed is equal to AG_c.
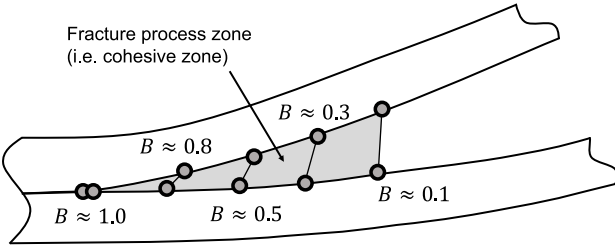

Fig. 5. Conventional CZM with fine modelling represented for a 50% mixed-mode ratio. Several elements are needed inside the fracture process zone.

mentioned that no discontinuity is present along the element length due to the linear element formulation.

Finally, approaching the total decohesion moment t_c, under constant mixed-mode ratio, self-similar growth is observed in practice with $\Delta_I = \Delta_I^f$ and $\Delta_{II} = \Delta_{II}^f$.

2.4. Energy motivation for the cohesive law

One of the principal motivations for the chosen damage formulation is that it should dissipate the correct amount of energy. In the following, this energy is derived as a function of the damage D. The energy from the dissipation mechanism can be expressed as the total work energy minus the reversible elastic energy

$$\mathcal{G} = \int_{t_a}^{t} \boldsymbol{F}^{\mathrm{T}} \dot{\boldsymbol{\Delta}} dt - \frac{1}{2} \boldsymbol{F}^{\mathrm{T}} \boldsymbol{\Delta}, \tag{13}$$

where $\boldsymbol{F} = \begin{bmatrix} F_I & F_{II} \end{bmatrix}^{\mathrm{T}}$, $\boldsymbol{\Delta} = \begin{bmatrix} \Delta_I & \Delta_{II} \end{bmatrix}^{\mathrm{T}}$, t is the current time, t_a is the time at which the cohesive law is initiated ($D = 0$) and $\dot{\cdot}$ represents derivative with respect to time. By assuming monotonic loading $\left(\text{i.e. } \frac{\Delta_a}{\Delta_a^{max}} = 1 \right)$, Eq. (8) becomes:

$$\boldsymbol{F} = \boldsymbol{F}^0 (1 - D). \tag{14}$$

Introducing this into the expression of the dissipated energy leads to:

$$\mathcal{G} = \int_{t_a}^{t} (1 - D) \boldsymbol{F}^{0\mathrm{T}} \dot{\boldsymbol{\Delta}} dt - \frac{1}{2} (1 - D) \boldsymbol{F}^{0\mathrm{T}} \boldsymbol{\Delta}. \tag{15}$$
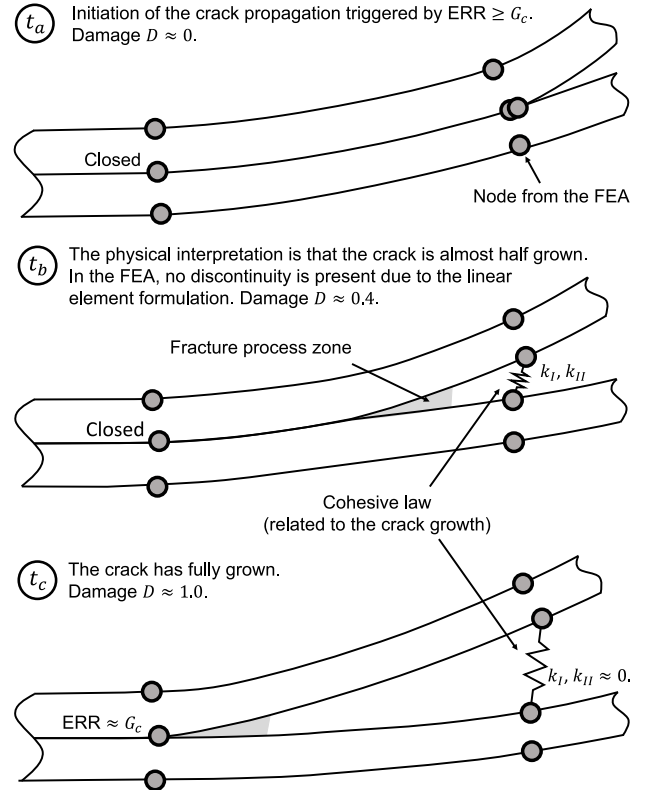

Fig. 6. Present crack propagation modelling. The crack propagation is triggered by the ERR estimation. A cohesive law is introduced to model the crack propagation along the length of the element. The cohesive law is related to the crack growth and not to the FPZ.

By setting

$$D = \frac{\boldsymbol{F}^{0\mathrm{T}} \boldsymbol{\Delta}}{2AG_c} = \frac{F_I^0 \Delta_I + F_{II}^0 \Delta_{II}}{2AG_c}, \tag{16}$$

the energy is expressed as a function of D with

$$\mathcal{G} = 2AG_c \left(\int_{t_a}^{t} (1 - D) \dot{D} dt - \frac{1}{2} (1 - D) D \right). \tag{17}$$

(a) Mode I representation.
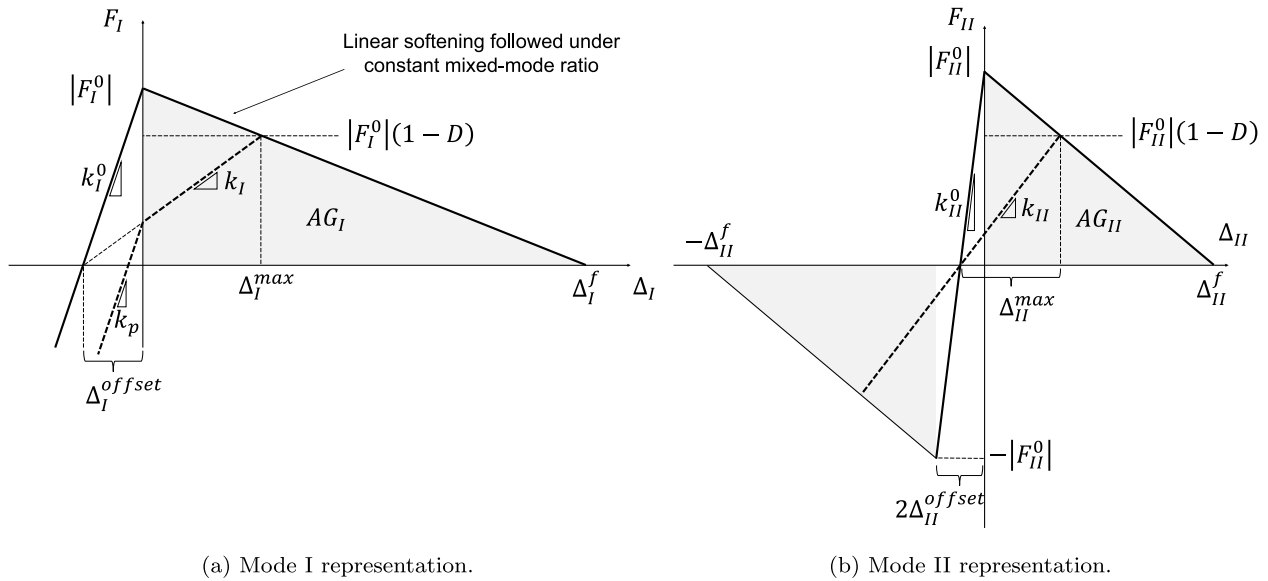

(b) Mode II representation.

Fig. 7. Force-opening representation of the cohesive law with initial opening offset. The offset ensures the initial stiffness to have a finite value.

Integrating per part and recalling that $D = 0$ at t_a, the expression simplifies to

$$\mathcal{G} = AG_c D. \tag{18}$$

The derivations above show that the damage variable in Eq. (16) ensures to dissipate the appropriate energy AG_c up to $D = 1$. By introducing Eqs. (7) and (11) into Eq. (16), and knowing that $G_c = G_T$, D can be expressed equivalently as

$$D = (1 - B) \frac{\Delta_I}{\Delta_I^f} + B \frac{\Delta_{II}}{\Delta_{II}^f}. \tag{19}$$

This expression is closer to the one exposed in Section 2.2 but some differences remain.

First, to avoid non-physical healing of the cohesive law, the maximum of d over time is taken in Eq. (10). It allows to substitute the initial monotonic loading assumption by the one in which both Δ_I and Δ_{II} are unloading and reloading at the same rate. In other words, when the maximum value of d is reached for the second time, it is done with the same values of Δ_I and Δ_{II} as the first time.

The second difference between Eqs. (9) and (19) is that the former presents Macaulay brackets. They have been introduced to exclude the contribution of mode I compression into the damage. From an energy point of view, it represents excluding from the dissipated cohesive energy the part corresponding to an anti-penetration force.

Finally, the last difference is the absolute values which have been introduced to avoid negative contribution to the damage variable. This change is motivated by the assumption that the shear damage behaves in a symmetric way, thus the cohesive law damages equally for negative and positive values of Δ_{II}.

Eq. (18) shows that the chosen damage variable ensures the cohesive law to dissipate the appropriate energy AG_c proportionally to the damage D. This is coherent with the idea that the variable D is related to the proportion of the elemental area currently opened. Finally, it is recalled that Eq. (18) stands for any monotonic path followed by the openings Δ_I and Δ_{II}.

2.5. Avoiding an infinite stiffness

The cohesive law presented in Section 2.2 is the proposed physical model to represent crack growth with large elements. However, an adaptation needs to be made for its implementation in FEA software.

By associating the interface stiffness to a spring–mass system, the stable time step in mode α can be expressed as

$$\delta t_\alpha = b \sqrt{\frac{m}{k_\alpha}}, \tag{20}$$

where m is the effective mass and b is a coefficient depending on the stiffness of the connected elements. Since the initial stiffness of the cohesive law k_α is infinite, it would result in a stable time step being null.

The proposed solution is to introduce an initial opening offset to the cohesive law. A similar procedure can be observed in [26]. This is done by setting:

$$F_I = \frac{\left|F_I^0\right|}{\Delta_I^{max}} (1 - D) \left(\langle \Delta_I \rangle + \Delta_I^{offset}\right) - k_p \langle -\Delta_I \rangle, \tag{21a}$$

$$F_{II} = \frac{\left|F_{II}^0\right|}{\Delta_{II}^{max}} (1 - D) \left(\Delta_{II} + \Delta_{II}^{offset}\right), \tag{21b}$$

where k_p is a penalty contact stiffness and Δ_α^{offset} is defined as

$$\Delta_\alpha^{offset} = \frac{F_\alpha^0}{k_\alpha^0}, \tag{22}$$

with k_α^0 being the initial stiffness either set as a user input or defined with Eq. (20) for a certain stable time step. Δ_I^{max} and Δ_{II}^{max} naturally become:

$$\Delta_I^{max} = \max_{\tau \in [0,t]} \left\langle \Delta_I(\tau) + \Delta_I^{offset} \right\rangle, \tag{23a}$$

$$\Delta_{II}^{max} = \max_{\tau \in [0,t]} \left| \Delta_{II}(\tau) + \Delta_{II}^{offset} \right|, \tag{23b}$$

with Δ_I^{max} being initialised to $|\Delta_I^{offset}|$ to account for cases where Δ_I^{offset} is negative. The initial non-zero value of Δ_α^{max} allows for an initial finite stiffness in Eq. (12).

Due to the introduction of the offsets, the damage function has to be adapted such that

$$d = (1 - B) \frac{\langle \Delta_I^* \rangle}{\left|\Delta_I^f\right|} + B \frac{\langle \Delta_{II}^* \rangle}{\left|\Delta_{II}^f\right|}, \tag{24}$$

with

$$\Delta_I^* = \left\langle \Delta_I + \Delta_I^{offset} \right\rangle - \left|\Delta_I^{offset}\right|, \tag{25a}$$

$$\Delta_{II}^* = \left|\Delta_{II} + \Delta_{II}^{offset}\right| - \left|\Delta_{II}^{offset}\right|. \tag{25b}$$

An illustration of the cohesive law with opening offset is presented in Fig. 7. The value of Δ_α^{offset} should be much smaller than Δ_α^f in order to ensure that the energy balance is not significantly altered in unloading cases. It is worth mentioning that the offset could be progressively reduced once the interface starts degrading.

3. Implementation

The ERR-Cohesive model has been implemented as a user subroutine for dynamic explicit integration scheme into the commercial FEA software LS-DYNA [20]. In the following, the adaptive element framework in which this implementation has been conducted is summarised. Then, some key aspects of the employed procedure are explained.

3.1. Framework

The present work is part of a wider strategy to model the damaging process of layered FRPs in large structures. A part of this strategy is to use an adaptive modelling approach previously published [21,22]. The simulation starts in an unrefined state with a single through-the-thickness linear solid-shell element defined by 8 base nodes. To be specific, LS-DYNA's reduced integration thick shell ELFORM 5 is used. During the simulation, the model can – where necessary – be refined through the thickness with weak (strain) discontinuities or strong (displacement jump) discontinuities. This is achieved by respectively adding 4 or 8 new nodes at the appropriate ply interface. The laminate is suitably split between the newly defined lower and upper elements. In order to know where to refine the model, a method has previously been developed to reliably detect possible delamination in linear elements [23]. Finally, the model presented in this article aims to be used as a method to describe the propagation of already initiated cracks. Naturally, the model has been implemented in the adaptive element subroutine mentioned.

For development and validation purposes, only the final state of the adaptive procedure (where the model is already refined with a strong discontinuity) is used in the present work. Additionally, only mode I and mode II are considered with a clear crack propagation direction. In order to model a bonded interface, the nodes at the strong refinements are coincident in space and tied together by imposing equal acceleration on both nodes [21]. If a cracked interface is to be modelled, the refined nodes are set free from each other and a frictionless penalty contact is introduced. An illustration of the initial state of refinement for the present study is presented in Fig. 8(a).

3.2. Procedure

One key aspect of the numerical procedure is the constraint method applied at the bonded region and the computation of the crack tip forces needed in the VCCT. The tied condition is ensured by a kinematic constraint equalling the acceleration of both nodes of the interface:

$$\ddot{u}^- = \ddot{u}^+, \tag{26}$$

where the superscripts $-$ and $+$ are respectively associated to the node of the lower and upper sub-laminate. By assuming a lumped mass matrix, a mass proportional damping and the absence of external forces, the acceleration condition can be ensured by distributing the sum of the internal elemental force of the lower and upper sub-laminates $(f^- + f^+)$ proportionally to the node masses m^- and m^+ [21]. The forces allocated to the node of the lower sub-laminate become

$$F^- = \kappa^- \left(f^- + f^+ \right), \tag{27}$$

where $\kappa^- = \frac{m^-}{m^- + m^+}$. The equivalent is done for the forces at the upper node F^+. For more details on the tied procedure, refer to [21].

The force at the lower node can be rearranged to make appear the interfacial force F^{tied} responsible for keeping the nodes coincident:

$$F^- = f^- + F^{tied}, \tag{28}$$

(a) Side view.
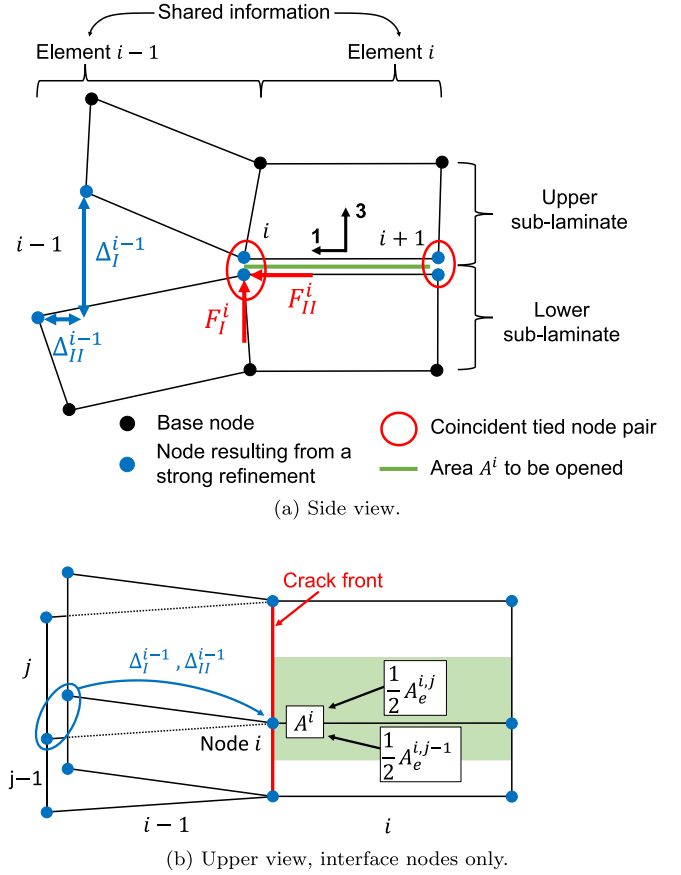

(b) Upper view, interface nodes only.

Fig. 8. Crack tip configuration in the adaptive element procedure. Each element is composed of 8 base nodes and 8 extra nodes to represent the crack interface. The opening, internal force and area information is shared between elements to compute the ERR by means of the VCCT.

with

$$F^{tied} = -\left(1 - \kappa^-\right) f^- + \kappa^- f^+. \tag{29}$$

These forces, oriented in the local crack tip coordinate system as shown in Fig. 8(a), are directly used in the ERR estimation with $F_I = F_3^{tied}$ and $F_{II} = F_1^{tied}$. Opposite forces would be found if calculated at the upper node.

Another aspect of the present procedure is the estimation of the area A^i associated to the node opening. A simple procedure is employed here for a single direction of crack propagation. At each node of the crack front, a loop over the connected elements is performed. Elements in front of the crack tip contribute with half of their elemental area $A_e^{i,j}$ such that

$$A^i = \frac{1}{2} \left(A_e^{i,j} + A_e^{i,j-1} \right). \tag{30}$$

An illustration is shown in Fig. 8(b). The nodes at the edges will receive area contribution from one element only. This simple procedure allows to account for irregular element widths. It should be reminded here that the irregularity in element length (in the crack direction) is taken into account by the shape correction factor c_α^i in Eq. (2).

These procedures are fed with adjacent elemental history variables through a built-in user subroutine in LS-DYNA. The latter allows to sync non-local information between neighbouring elements distributed in different memory partitions (computational nodes). The shared information is the elemental forces, the node openings, the elemental area at the interface and the tied status of the nodes.

4. Numerical examples

In this section, a numerical validation of the presented ERR-Cohesive method is carried out with standard delamination propagation tests. DCB, ENF and MMB tests have been simulated with regular meshes for various element lengths. It demonstrates the ability of the method in modelling delamination propagation with large elements. In the case of the DCB, a comparison with cohesive elements is presented. Afterwards, the same cases are presented with irregular mesh sizes to discuss about the accuracy of the VCCT shape correction factor presented in Section 2.1.

4.1. Description of the propagation tests

Standard DCB, ENF and MMB tests have been used respectively for pure mode I, pure mode II and 3 mixed-mode configurations ($B = 0.2$, $B = 0.5$ and $B = 0.8$). The dimensions and material properties are extracted from a benchmark proposed by Krueger [27]. They are summarised respectively in Fig. 9 and Table 1. The laminate is made of unidirectional carbon-FRP layers, aligned in the longitudinal direction of the coupons. In order to ensure stable crack growth, the initial crack lengths have been adapted to $a_0 = 0.7L$ for ENF and to $a_0 = 0.67L$ for the MMB case (where $B = 0.8$).
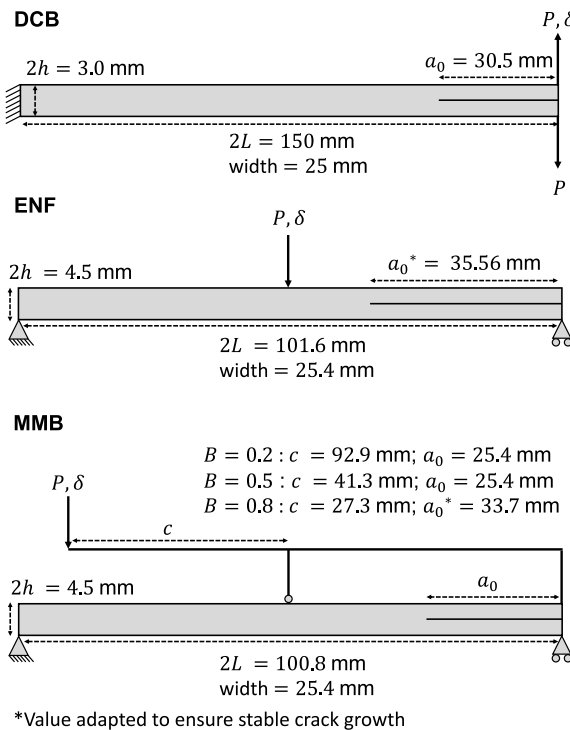

DCB

$2h = 3.0$ mm
$a_0 = 30.5$ mm
P, δ
$2L = 150$ mm
width = 25 mm
P

ENF

P, δ
$2h = 4.5$ mm
$a_0^* = 35.56$ mm
$2L = 101.6$ mm
width = 25.4 mm

MMB

$B = 0.2 : c = 92.9$ mm; $a_0 = 25.4$ mm
$B = 0.5 : c = 41.3$ mm; $a_0 = 25.4$ mm
$B = 0.8 : c = 27.3$ mm; $a_0^* = 33.7$ mm
P, δ
c
$2h = 4.5$ mm
a_0
$2L = 100.8$ mm
width = 25.4 mm

*Value adapted to ensure stable crack growth

Fig. 9. Benchmark configurations used for the numerical validation [27].

Table 1
Material properties used in the benchmark tests [27].

Property	DCB	ENF/MMB	Units
Material	T300/1076	IM7/8552	
E_{11}	139.4	161.0	GPa
$E_{22} = E_{33}$	10.16	11.38	GPa
$G_{12} = G_{13}$	4.6	5.2	GPa
G_{23}	3.54	3.9	GPa
$\nu_{12} = \nu_{13}$	0.30	0.32	–
ν_{23}	0.436	0.45	–
G_{Ic}	0.170	0.212	kJ m^{-2}
G_{IIc}	0.494	0.774	kJ m^{-2}
η	1.62	2.1	–
ρ^a	1500	1500	kg m^{-3}

^{a}Not specified in [27], a standard value is used.

The simulations have been calculated with element lengths of about 2 mm, 4 mm and 8 mm. In order to respect the coupon dimensions while keeping a regular mesh, the exact element lengths slightly differ throughout the different tests. Such mesh sizes have been chosen to show the ability of the method in modelling delamination propagation with element larger than the FPZ.

The results are compared with the analytical ones based on the Corrected Beam Theory (CBT) [28–30]. In the case of the MMB tests with $B = 0.5$ and $B = 0.8$, the results from the benchmark by Krueger are also presented for $a > L$.

The load is introduced through an imposed displacement following a sinusoidal shape with a termination time of 0.5 s. It should be noted that no damping has been introduced to the model. To show the unloading capability of the present method, the simulations with a mesh size of 4 mm are unloaded and reloaded at about half of the imposed displacement. It has been ensured that it corresponds to a moment where the cohesive law is active at the crack tip.

The stiffnesses $k_I^0 = k_{II}^0$ have been defined to ensure a stable time step at the interface of 0.25 µs, by using Eq. (20) with $b = 0.9\sqrt{2}$ (where $b = \sqrt{2}$ is a value which has shown stability and 0.9 is a safety coefficient). Examples of resulting stiffness and opening offset are presented for the DCB and ENF cases in Table 2. It is worth noting that, for the same interface stable time step, the ratio $\Delta_I^{offset}/\Delta_I^f$ decreases greatly for larger elements.

Table 2
Obtained values of stiffnesses $k_I^0 = k_{II}^0$, opening offset $|\Delta_\alpha^{offset}|$ and ratio of opening offset to failure opening $\Delta_\alpha^{offset}/\Delta_\alpha^f$ for the DCB and ENF cases. The stiffness k_α^0 has been determined using Eq. (20) with $b = 0.9\sqrt{2}$ to ensure a stable time step at the interface of 0.25 µs.

	Element length	$k_I^0 = k_{II}^0$ (kN mm^{-1})	$|\Delta_\alpha^{offset}|$ (mm)	$\Delta_\alpha^{offset}/\Delta_\alpha^f$
DCB $\alpha = I$	2 mm	62.2	0.75×10^{-3}	2.38%
	4 mm	248.9	0.31×10^{-3}	0.42%
	8 mm	995.6	0.11×10^{-3}	0.06%
ENF $\alpha = II$	2 mm	86.6	6.58×10^{-3}	60.04%
	4 mm	346.5	3.37×10^{-3}	15.75%
	8 mm	1385.8	1.79×10^{-3}	4.43%

4.2. Double cantilever beam (DCB)

The DCB results in Fig. 10 show high accuracy of the present method when comparing to the analytical solution. The ERR is well predicted for all the mesh sizes. Further, the associated cohesive law allows to smoothly propagate the crack along the element length with no visible instabilities. By looking closely, a first discontinuity can be seen before the peak-load is reached. This is due to the ERR being triggered first at the middle (width direction) of the coupon. The peak load is reached when the extremities of the crack front open as well. These discontinuities repeat each time a new row of elements is encountered by the crack front. Finally, the unloading and reloading behaves as expected as illustrated by the results for the 4-mm mesh.

As a comparison, results with conventional CZM are presented in Fig. 11. The material formulation MAT_138 from LS-DYNA [20] is used. A prototype values of 30 MPa have been considered for the mode I strength. When using a fine mesh of 0.25 mm, the difference with the CBT solution is small. However, for the 2-mm and 4-mm mesh, the CZM overestimates the initial force at which the crack starts propagating. This is due to the FPZ being much smaller than the element length. When using a reduced strength, as proposed by Turon et al. [3], the initial response of the DCB is much softer than the LEFM one. Additionally, the peak load is greatly underestimated. By comparing the results of the 2-mm and 4-mm meshes, one can see that these limitations worsen rapidly when increasing the element's length.

A summary of the compared modelling methods, associated FPZ sizes and element lengths is presented in Table 3. Here, the FPZ have been estimated with the expression for linear softening by Soto et al. [4].
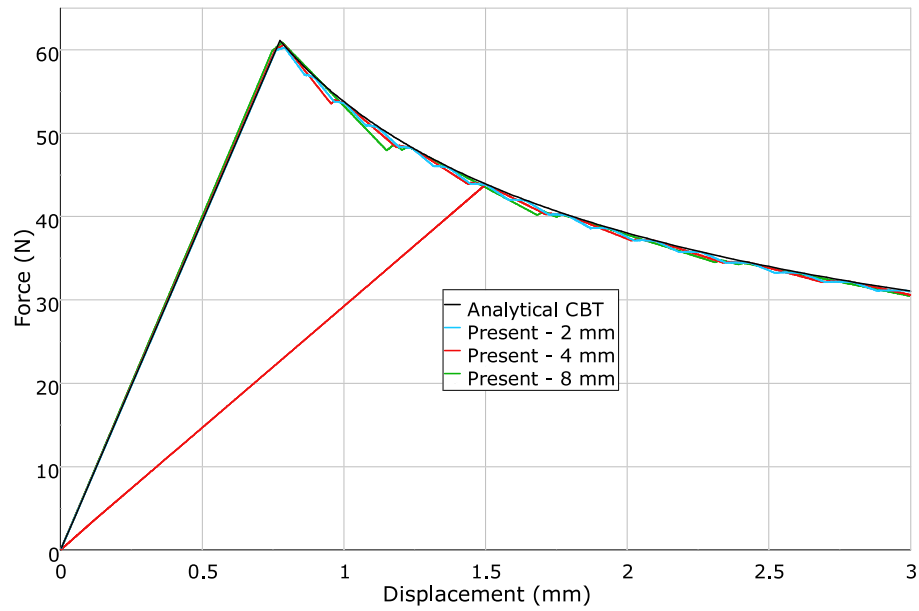
Fig. 10. DCB results for 3 sizes of regular meshes. Note that the curve for the 4-mm mesh includes loading and reloading.
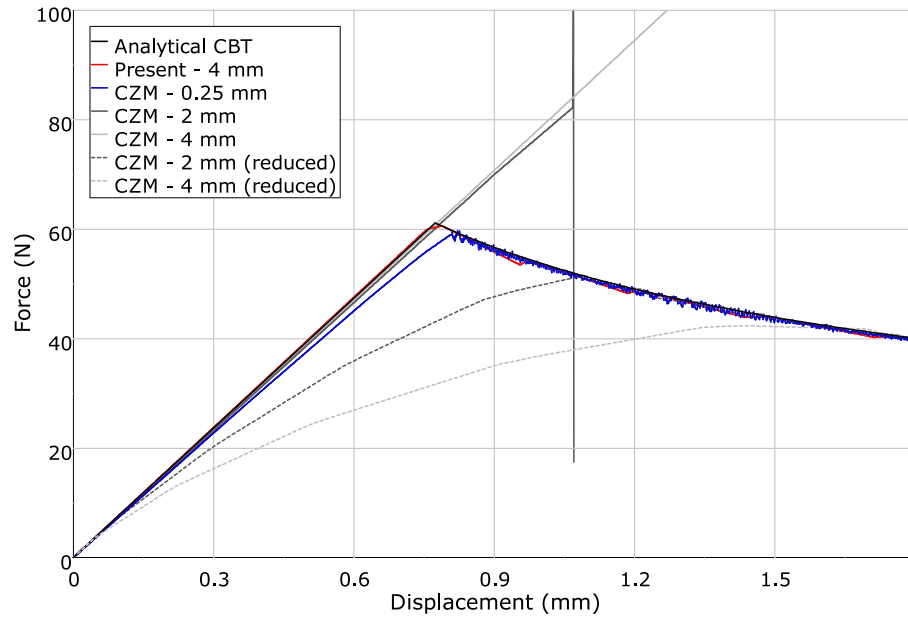

Fig. 11. DCB results with conventional cohesive zone modelling. The strengths used and their associated FPZ sizes are summarised in Table 3. For comparison, the results of the 4-mm mesh with the present method are also plotted. Due to large vibrations, the results for the 2-mm mesh CZM are not plotted further than the initiation of propagation.

Table 3

Comparison between the element length and the size of the FPZ for the compared DCB modelling strategies. The length of the FPZ is estimated with the expression from Soto et al. [4]. For CZM with reduced strength, the strength X_I has been lowered such that 3 elements are present in the FPZ.

Modelling method	Strength X_I (MPa)	FPZ size (mm)	Element length (mm)
ERR-Cohesive (Present)	–	–	2.08, 4.17 and 8.33
CZM typical X_I	30	0.80	0.25, 2.08 and 4.17
CZM reduced X_I	2.05 0.54	6.25 12.5	2.08 4.17

4.3. End-notched flexure (ENF)

The results for the ENF configuration are shown in Fig. 12. Accurate mode II propagation is observed. Compared with the analytical solution, a slightly higher force is observed from $a = a_0$ (first discontinuity) to $a = L$ (second discontinuity). On the contrary, a slightly lower force is observed for $a > L$. These small differences are expected to come from the full width representation of the coupon in the FEA differing from the 2D analytical consideration of the CBT.

Additionally, some irregularities can be seen around a displacement of 1.5 mm, corresponding to the crack tip reaching the point of application of the load, i.e. $a = L$. At this instant, the large elements prevent modelling the transition smoothly. Furthermore, similarly to the DCB, unloading and reloading is properly handled, as indicated by the results for the 4 mm mesh where the force curve goes back to the origin before reloading along the same path.
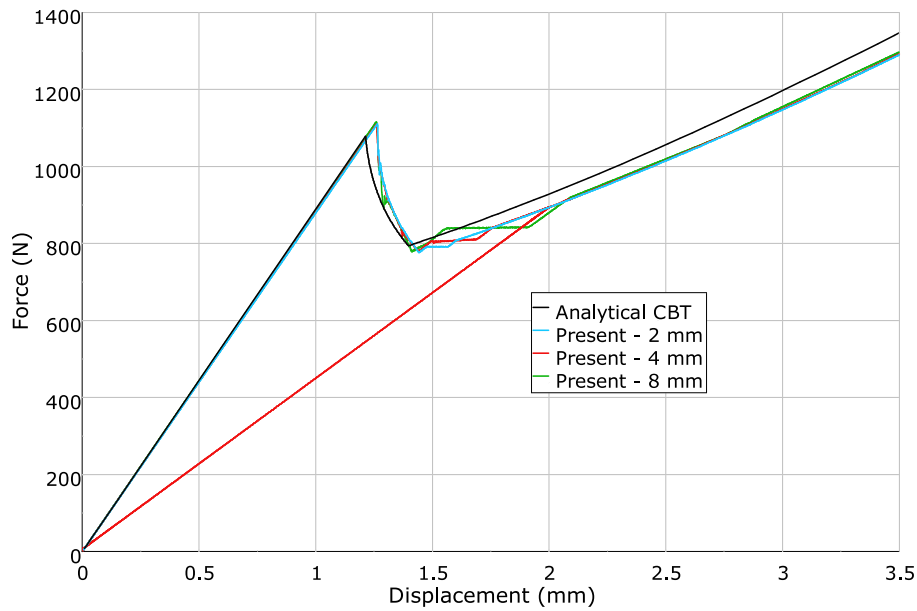
Fig. 12. ENF results for 3 sizes of regular meshes. Note that the curve for the 4-mm mesh includes loading and reloading.
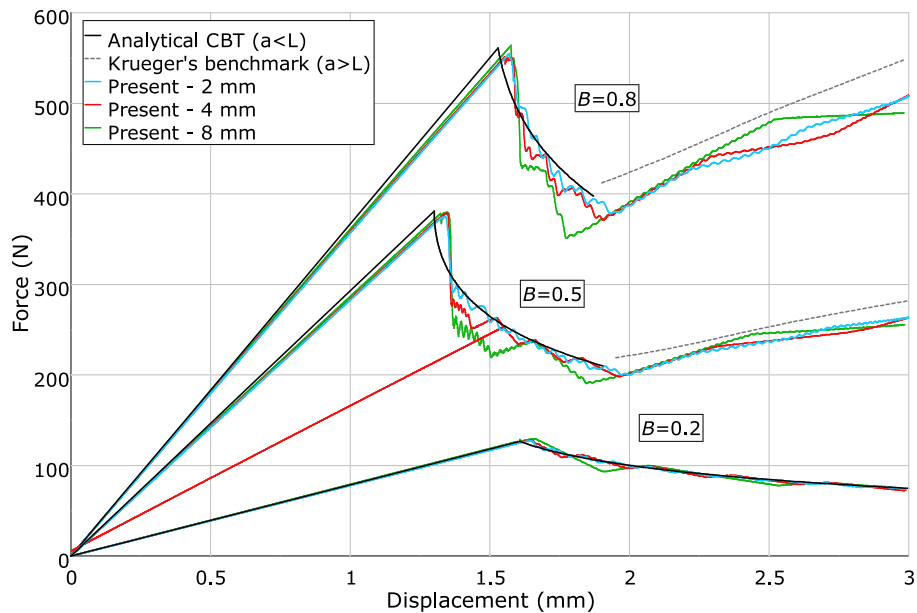

Fig. 13. MMB results for 3 sizes of regular meshes. 3 mode ratios are presented: $B = 0.2$, $B = 0.5$ and $B = 0.8$. Note that the curve for the 4-mm mesh, with $B = 0.5$, includes loading and reloading.

4.4. Mixed-mode bending (MMB)

The results for three different mixed-mode ratios are presented in Fig. 13. It appears that the VCCT accurately predicts the proper mode-mixity. Further, it is also shown that the present ERR-Cohesive method is able to dissipate the correct amount of energy. It is recalled that only one row of elements at a time is modelling the progressive damage propagation.

The curves corresponding to the 2-mm meshes are closely following the analytical solutions. Even if the coarser discretisation of the 8 mm meshes leads to larger discontinuities, the results can be considered acceptable. Generally, some small vibrations can be observed due to the MMB test having poor stability in dynamic modelling. The unloading and reloading, for $B = 0.5$, presents the expected results as well under mixed-mode loading.

4.5. Results for irregular mesh size

Considering that element size variations are common in the industry to represent complicated geometry, it appears relevant to validate the present method in such conditions. As explained in Section 2.1, to obtain a reliable ERR estimation with the VCCT when different element lengths are present ahead and behind the crack front, the shape correction factors of Eq. (4) are used.

The tests previously presented with regular meshes have been modelled with mesh size variations. Two configurations are considered, see Fig. 14. For the DCB and ENF tests, the mesh length is alternating, in the longitudinal direction, between 2 mm and 4 mm for the first configuration and between 4 mm and 8 mm for the second configuration. In the case of the ENF test, the second configuration uses sizes of 3 mm and 6 mm to be compatible with the dimensions of the coupon. In the
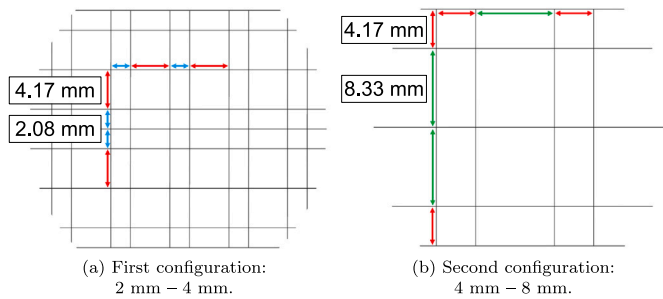
(a) First configuration: 2 mm − 4 mm.

(b) Second configuration: 4 mm − 8 mm.

Fig. 14. Irregular mesh configurations used for the validation of the shape correction factors and area procedures. In the longitudinal direction, shorter and longer elements are alternated. In the transverse direction, the width alternates every two elements. The length values exposed are for the DCB test.

width direction, the mesh length is alternating in the same way, but for every two consecutive elements, such that the area associated to each node pair varies along the crack front. In all the cases, a length ratio of 2 is used between the larger and the shorter elements.

The results for the DCB case with irregular meshes are shown in Fig. 15. The curves with the present shape correction factor are in agreement with the analytical one. However, it can be seen that the ERR is slightly overestimated at the initial crack length, meaning that the initial crack propagation (peak load) is predicted with a slightly lower force. Once the crack has propagated along the length of the first element, the mesh configuration is reversed and the ERR is slightly underestimated. It should be noted that these small errors are similar in both element lengths used. Finally, a stable crack propagation is observed.

For comparison, the results for the linear shape correction factor found in the literature are shown in light and dark grey. It can be seen that the ERR estimation error is much greater. It is worth noting that the error is greater for the 4 mm–8 mm configuration than the 2 mm–4 mm configuration. It demonstrates that the assumption of linear growth of the opening with respect to the distance to the crack tip is not valid with large elements. In both configurations, these large errors result in large vibrations. It is concluded that the presented correction factor is preferable.

The simulations for ENF and MMB with $B = 0.5$ are presented in Fig. 16. The good results illustrate the accuracy of the present shape correction factor for mode II and mixed-mode propagation. It should be reminded that the mode II correction factor used here is the linear one found in the literature. Although small vibrations appear, it demonstrates that the linear correction can be used with large element in mode II.

5. Conclusions and outlook

5.1. Conclusions

In this paper, an ERR-Cohesive method to efficiently model delamination propagation in composite materials has been presented. The method estimates the energy release rate at the crack front by means of the VCCT. When the ERR exceeds the fracture toughness of the material, the delamination is propagated further. A cohesive law is then introduced to progressively release the entire interface along the length of the element.

The novel cohesive formulation presented ensures the dissipation of the appropriate amount of energy, corresponding to the global mode mixity, for any monotonic evolution of the openings. The coupled damage variable allows to obtain a reliable behaviour under mixed-mode loading.

Compared to traditional cohesive zone modelling, which needs a fine discretisation, the presented method can be used with elements

that are much larger than the fracture process zone. Therefore, the method is efficient in the sense that it can be used with large elements. The modelling of the progressive damage is carried out by a single element in the direction of propagation. The interface starts degrading from a non-null interface force, which avoids adding initial artificial compliance.

The novel method has been used to model DCB, ENF and MMB tests with regular and irregular meshes. The results are in agreement with the analytical solutions for the 3 element lengths used: 2 mm, 4 mm and 8 mm. The ability of the presented ERR-Cohesive method to propagate delamination with large elements opens possibilities to accurately model delamination in large structures. It is especially suited for the industries where entire vehicles are represented in the FEA.

5.2. Outlook

Ensuring a sufficiently large stable time step is critical for the ability to model large structures in dynamic FEA solvers with explicit integration schemes. A typical stable time step of 0.5 μs can currently be found in the automotive industry. Such stable time steps are usually incompatible with conventional CZM due to the fine discretisation and high stiffness needed (to avoid adding artificial compliance).

In the present modelling strategy, large in-plane element stable time step can be reached since large elements can be used. Nevertheless, in some cases, a relatively high stiffness is also needed to ensure a low value of Δ_α^{offset}, thus limiting the interface stable time step. However, the method could offer two reasonable ways to alleviate this limitation. First, since no artificial compliance is initially added to the model, by assuming monotonic loading, k_α^0 could be lowered. Second, because the cohesive law is present at the crack front only, the mass could be artificially increased locally. Both resulting in a larger stable time step.

The present ERR-Cohesive method has been presented in the frame of a near 2D configuration where the crack propagates in a clear direction. The procedure would need further adaptations in order to propagate the crack front in the correct direction of the plane. Additionally, the crack front would have to propagate in cases where it is not aligned with the mesh. Future works could focus on the generalisation of the method to arbitrary crack growth.

The VCCT relies on the existence of a crack in order to compute the energy release rate. Therefore, the initial crack opening is another aspect to be solved on the way toward a complete delamination strategy for large structures. A previously published work by the authors [23] has shown the possibility to accurately compute transverse stresses in linear shell elements. Therefore, opening possibilities for a stress-based criterion to initiate new cracks. The transition from a closed to an open crack could, in such a case, be ensured by the cohesive law presented in this article.

With these further developments, the proposed method can formulate an effective strategy to model delamination failure in large structures.

CRediT authorship contribution statement

Pierre M. Daniel: Conceptualization, Software, Investigation, Validation, Writing – original draft, Writing – review & editing , Visualization. **Johannes Främby:** Conceptualization, Software, Validation, Writing – review & editing. **Martin Fagerström:** Conceptualization, Validation, Supervision, Writing – review & editing. **Pere Maimí:** Conceptualization, Validation, Supervision, Writing – review & editing, Funding acquisition.

Declaration of competing interest

The authors declare that they have no known competing financial interests or personal relationships that could have appeared to influence the work reported in this paper.
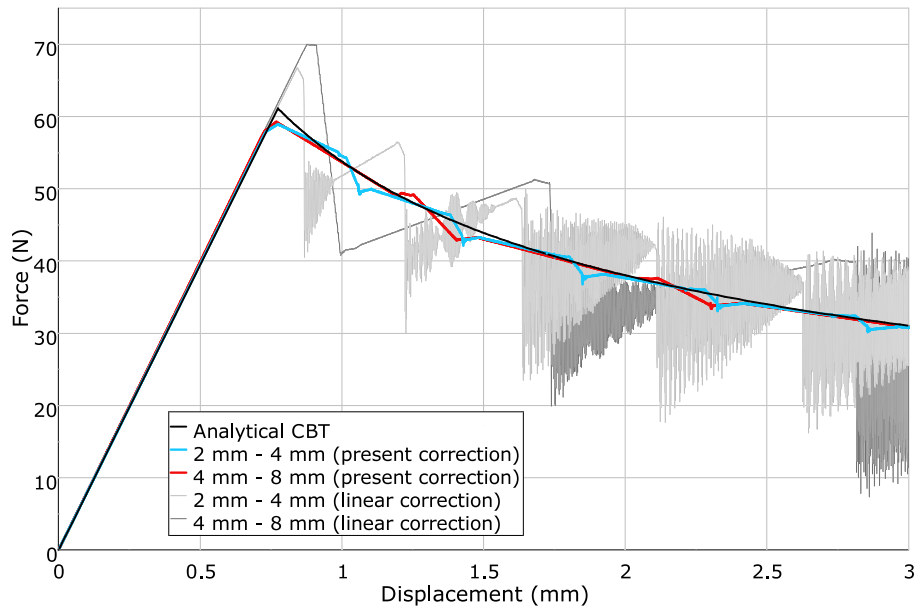
Fig. 15. DCB results with irregular mesh configurations, where results from using the proposed shape correction factor are also compared to results obtained with a classical linear correction.
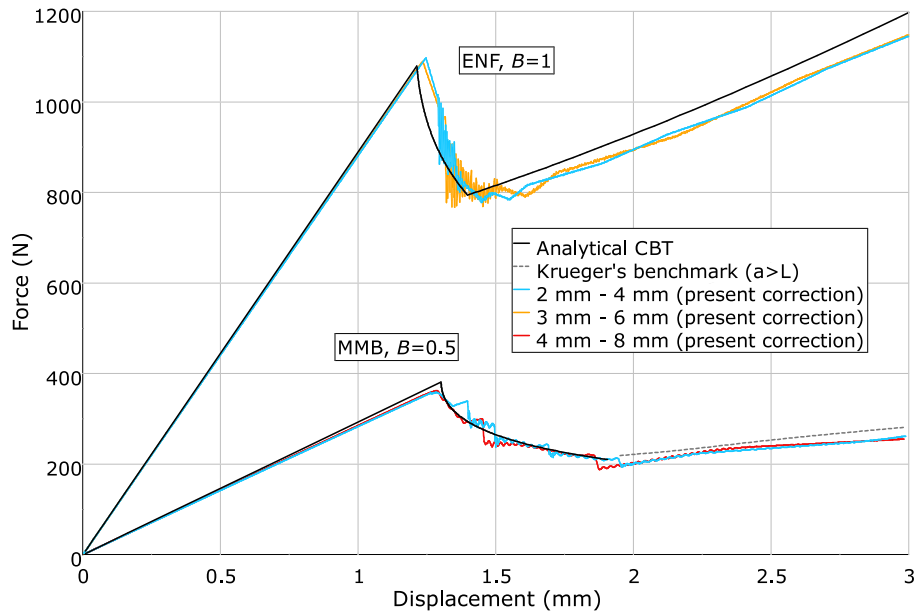

Fig. 16. ENF and MMB results with irregular mesh configurations using the proposed shape correction factors.

Data availability

The authors do not have permission to share data.

Acknowledgements

Appendix. Opening correction for dissimilar element lengths

As explained in Section 2.1, the opening Δ^{i-1} measured behind the crack must be corrected when the element lengths are different on each side of the tip in order to comply with the self-similar growth assumption. This section aims to express the correction factor c_α^i to be applied to the VCCT due to the variation of element length

$$c_\alpha^i = \frac{\Delta_\alpha^i}{\Delta_\alpha^{i-1}}. \tag{A.1}$$

Using the Timoshenko beam theory, the generalised strain $u_{,i}$ and $\theta_{,i}$ are expressed as a function of the normal force N and moment M
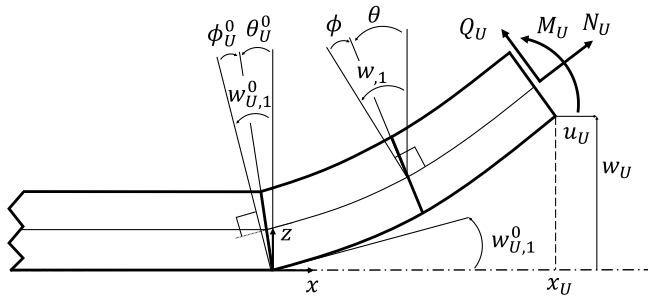
Fig. A.17. Crack tip representation of the upper arm according to Timoshenko beam theory.

by means of the inverse of the ABD matrix applied to the upper arm:

$$
\begin{bmatrix} u_{,i} \\ \theta_{,i} \end{bmatrix} = \begin{bmatrix} A_U & B_U \\ B_U & D_U \end{bmatrix} \begin{bmatrix} N \\ M \end{bmatrix}.
\tag{A.2}
$$

The rotation of the vertical section θ is expressed as

$$
\theta = w_{,1} + \phi,
\tag{A.3}
$$

where ϕ is the additional rotation of the section, due to transverse shearing, with respect to the beam axis orthogonal plane, see Fig. A.17. By combining Eqs. (A.2) and (A.3), inserting the transverse shear strain $\phi = -\gamma_{13} = -Q_U K_U$ and expressing the resultant stresses as functions of the upper arm loads $N = N_U$, $Q = Q_U$ and $M = M_U + Q_U (x_U - x)$, the following differential equations can be obtained:

$$
u_{,1} = A_U N_U + B_U \left(M_U + Q_U (x_U - x) \right),
\tag{A.4a}
$$

$$
\theta_{,1} = B_U N_U + D_U \left(M_U + Q_U (x_U - x) \right),
\tag{A.4b}
$$

$$
w_{,1} = \theta + K_U Q_U.
\tag{A.4c}
$$

After integration, inserting the expression of θ into w, considering that the displacement at the bottom of the beam is equal to the displacement at the mid-surface, and finally that at $x = 0$, $u = 0$, $w = 0$, $\theta = \theta_U^0$, the following is obtained:

$$
u_U = \left(A_U N_U + B_U \left(M_U + Q_U x_U \right) \right) x - B_U Q_U \frac{x^2}{2},
\tag{A.5a}
$$

$$
w_U = \left(\theta_U^0 + K_U Q_U \right) x + \left(B_U N_U + D_U \left(M_U + Q_U x_U \right) \right) \frac{x^2}{2} - D_U Q_U \frac{x^3}{6}.
\tag{A.5b}
$$

By applying the same reasoning to the lower arm and taking the difference, the openings are expressed as

$$
\Delta_I = w_U - w_L = \alpha_1 x + \alpha_2 x^2 + \alpha_3 x^3,
\tag{A.6a}
$$

$$
\Delta_{II} = u_U - u_L = \beta_1 x + \beta_2 x^2,
\tag{A.6b}
$$

with

$$
\alpha_1 = \theta^0 + K_U Q_U - K_L Q_L,
\tag{A.7a}
$$

$$
\alpha_2 = \frac{1}{2} \left(B_U N_U - B_L N_L + D_U \left(M_U + Q_U x_U \right) - D_L \left(M_L + Q_L x_L \right) \right),
\tag{A.7b}
$$

$$
\alpha_3 = \frac{1}{6} \left(D_L Q_L - D_U Q_U \right)
\tag{A.7c}
$$

$$
\beta_1 = A_U N_U - A_L N_L + B_U \left(M_U + Q_U x_U \right) - B_L \left(M_L + Q_L x_L \right),
\tag{A.7d}
$$

$$
\beta_2 = \frac{1}{2} \left(B_L Q_L - B_U Q_U \right),
\tag{A.7e}
$$

and where $\theta^0 = \theta_U^0 - \theta_L^0$.

In the literature, it is common to consider a linear correction with respect to the length of the element [13]. It is assumed that the linear part of the openings is predominant and that the higher terms can be neglected. With such an assumption, the correction factor becomes

$$
c_I^i = \frac{\alpha_1 l^i}{\alpha_1 l^{i-1}} = \frac{l^i}{l^{i-1}} = C,
\tag{A.8a}
$$

$$
c_{II}^i = \frac{\beta_1 l^i}{\beta_1 l^{i-1}} = \frac{l^i}{l^{i-1}} = C.
\tag{A.8b}
$$

This correction factor gives good results for small element lengths where the openings are dominated by the linear terms. However, when using large elements in mode I, the quadratic term is no longer negligible. Therefore, a correction factor considering the quadratic term is proposed here

$$
c_I^i = \frac{\alpha_1 l^i + \alpha_2 l^{i2}}{\alpha_1 l^{i-1} + \alpha_2 l^{i-12}},
\tag{A.9}
$$

which can be expressed as

$$
c_I^i = \frac{l^i}{\Delta_I^{i-1}} \alpha_1 (1 - C) + C^2,
\tag{A.10}
$$

from which Δ_I^{i-1}, l^i and C are known from the finite element analysis and α_1 needs to be evaluated. By assuming that the shear terms are negligible in the expression of α_1, it becomes equal to $\theta^0 = \theta_U^0 - \theta_L^0$ which can directly be measured in the analysis, see θ_U^0 in Fig. A.17. Finally, it is obtained

$$
c_I^i = \frac{l^i}{\Delta_I^{i-1}} \theta^0 (1 - C) + C^2.
\tag{A.11}
$$

A comparison between the linear and quadratic correction is presented for a DCB with irregular mesh lengths in Section 4.5. The accuracy of the linear correction for mode II propagation is also exposed.

References

[1] Davila CG, Camanho P, de Moura M. Mixed-mode decohesion elements for analyses of progressive delamination. In: 19th AIAA applied aerodynamics conference. (February). Reston, Virigina: American Institute of Aeronautics and Astronautics; 2001.

[2] Turon A, Camanho P, Costa J, Dávila C. A damage model for the simulation of delamination in advanced composites under variable-mode loading. Mech Mater 2006;38(11):1072–89.

[3] Turon A, Dávila C, Camanho P, Costa J. An engineering solution for mesh size effects in the simulation of delamination using cohesive zone models. Eng Fract Mech 2007;74(10):1665–82.

[4] Soto A, González E, Maimí P, Turon A, Sainz de Aja J, de la Escalera F. Cohesive zone length of orthotropic materials undergoing delamination. Eng Fract Mech 2016;159:174–88.

[5] Williams JG. On the calculation of energy release rates for cracked laminates. Int J Fract 1988;36(2):101–19.

[6] Suo Z, Hutchinson JW. Interface crack between two elastic layers. Int J Fract 1990;43(1):1–18.

[7] Davidson BD, Hu H, Schapery RA. An analytical crack-tip element for layered elastic structures. J Appl Mech 1995;62(2):294–305.

[8] Rice JR. A path independent integral and the approximate analysis of strain concentration by notches and cracks. J Appl Mech 1968;35(2):379–86.

[9] Ishikawa H, Kitagawa H, Okamura H. J-integral of a mixed mode crack and its application. In: Mechanical behaviour of materials. Vol. 3, (August):Elsevier; 1980, p. 447–55.

[10] Judt PO, Ricoeur A. Crack growth simulation of multiple cracks systems applying remote contour interaction integrals. Theor Appl Fract Mech 2015;75(October 2017):78–88.

[11] Irwin GR. Fracture. Vol. 970, (1951):1958, p. 551–90.

[12] Rybicki E, Kanninen M. A finite element calculation of stress intensity factors by a modified crack closure integral. Eng Fract Mech 1977;9(4):931–8.

[13] Krueger R. Virtual crack closure technique: History, approach, and applications. Appl Mech Rev 2004;57(2):109–43.

[14] McElroy M. An enriched shell finite element for progressive damage simulation in composite laminates. NASA/TP–2016-219211, 2016.

[15] Brambilla P, Bisagni C, Dávila CG. Modeling of delamination in composite structures under static and fatigue loading. (Master thesis), Politecnico Di Milano; 2012.

[16] Mabson GE, De Carvalho NV, Krueger R. VCCT with progressive nodal release for simulating mixed-mode delamination: Formulation, algorithmic improvements and implications. In: American society for composites 2018. Lancaster, PA: DEStech Publications, Inc.; 2018.

[17] Mabson G, Deobald L, Dopker B. Fracture interface elements for the implementation of the virtual crack closure technique. In: 48th AIAA/ASME/ASCE/AHS/ASC structures, structural dynamics, and materials conference. (April):Reston, Virigina: American Institute of Aeronautics and Astronautics; 2007, p. 1–11.

[18] Orifici AC, Thomson RS, Degenhardt R, Bisagni C, Bayandor J. Development of a finite-element analysis methodology for the propagation of delaminations in composite structures. Mech Compos Mater 2007;43(1):9–28.

[19] Zou Z, Reid S, Li S, Soden P. Application of a delamination model to laminated composite structures. Compos Struct 2002;56(4):375–89.

[20] LSTC, ANSYS Inc. LS-DYNA R11.1.0. 2019.

[21] Främby J, Fagerström M, Karlsson J. An adaptive shell element for explicit dynamic analysis of failure in laminated composites Part 1: Adaptive kinematics and numerical implementation. Eng Fract Mech 2020;240(February):107288.

[22] Främby J, Fagerström M. An adaptive shell element for explicit dynamic analysis of failure in laminated composites Part 2: Progressive failure and model validation. Eng Fract Mech 2021;244(October 2020):107364.

[23] Daniel PM, Främby J, Fagerström M, Maimí P. Complete transverse stress recovery model for linear shell elements in arbitrarily curved laminates. Compos Struct 2020;252(June):112675.

[24] Benzeggagh M, Kenane M. Measurement of mixed-mode delamination fracture toughness of unidirectional glass/epoxy composites with mixed-mode bending apparatus. Compos Sci Technol 1996;56(4):439–49.

[25] Turon A, Camanho P, Costa J, Renart J. Accurate simulation of delamination growth under mixed-mode loading using cohesive elements: Definition of interlaminar strengths and elastic stiffness. Compos Struct 2010;92(8):1857–64.

[26] Hille TS, Suiker AS, Turteltaub S. Microcrack nucleation in thermal barrier coating systems. Eng Fract Mech 2009;76(6):813–25.

[27] Krueger R. A summary of benchmark examples to assess the performance of quasi-static delamination propagation prediction capabilities in finite element codes. J Compos Mater 2015;49(26):3297–316.

[28] Reeder JR, Demarco K, Whitley KS. The use of doubler reinforcement in delamination toughness testing. Composites A 2004;35(11):1337–44.

[29] Allix O, Ladevéze P, Corigliano A. Damage analysis of interlaminar fracture specimens. Compos Struct 1995;31(1):61–74.

[30] Mi Y, Crisfield MA, Davies GAO, Hellweg HB. Progressive delamination using interface elements. J Compos Mater 1998;32(14):1246–72.